Fuel 196 (2017) 195–209

Contents lists available at ScienceDirect

Fuel

journal homepage: www.elsevier.com/locate/fuel

Full Length Article

Towards understanding the microstructural and structural changes in natural hierarchical materials for energy recovery: *In-operando* multi-scale X-ray scattering characterization of Na- and Ca-montmorillonite on heating to 1150 °C

Greeshma Gadikota [a,b,*], Fan Zhang [b], Andrew J. Allen [b]

[a] Department of Civil and Environmental Engineering, Princeton University, Princeton, NJ 08544, United States
[b] Materials Measurement Science Division, National Institute of Standards and Technology, Gaithersburg, MD 20899, United States

ARTICLE INFO

Article history:
Received 4 November 2016
Received in revised form 25 January 2017
Accepted 28 January 2017
Available online 7 February 2017

Keywords:
Na-montmorillonite
Ca-montmorillonite
Heat-treatment
Ultra-small angle X-ray scattering (USAXS)
Small angle X-ray scattering (SAXS)
Wide angle X-ray scattering (WAXS)
Microstructure
Morphology
Crystal structure
Multi-scale characterization
Sintering

ABSTRACT

Understanding the changes in the microstructures and structures of clays with varying intercalated metal ions at elevated temperatures is of importance for many applications ranging from the recovery of shale gas from unconventional formations to developing effective nuclear waste containment technologies, and engineering materials such as ceramics for fuel cell applications. In this study, synchrotron-based *in-operando* multi-scale X-ray scattering analyses are used to determine dynamic microstructural and crystal structural changes in Na- and Ca-montmorillonite on heating from 30 °C to 1150 °C. Larger cations such as Ca^{2+} confer more defined morphological regimes compared to Na^{+} ions in compacted clays, as evident from the ultra-small-angle X-ray scattering results. The hierarchical morphology of clays is characterized to distinguish between nano-scale interlayer swelling porosity, meso-scale porosity, and intergranular pore spaces between powdered clay grains. On heating from ambient temperature to 200 °C, the removal of interlayer water reduced the basal distances to 9.6 Å. On further heating to 800 °C, gradual dehydroxylation of the clay sheets is evident from the structural changes. The effects of sintering at temperatures greater than 800 °C are evident from significant reductions in the intrinsic porosities of the clay sheets, and the formation of newer phases such as mullite. By connecting the *in-operando* microstructural and structural changes across spatial scales ranging from micrometers to Angstroms, the possibility of engineering high temperature processes for achieving morphologies and chemical compositions of interest is presented.

1. Introduction

A fundamental microstructural and crystal structural understanding of clays at elevated temperatures is essential for the advancement of many technologies related to materials science, and energy and environment such as the development of effective well-bore sealants for drilling applications [1], robust clay barriers for effective nuclear waste containment [2], novel ceramic fuel cell materials [3], gas storage and transport at elevated temperatures [4,5], and enhancing the sorption of heavy radioactive metals into clay structures [6]. While various studies have investigated the microstructures [7–14], or the crystal structures of clays [15–17], there remains a limited scientific understanding of how changes at the nano-scale impact the microstructural properties, or vice versa.

Several recent advances in synchrotron-based X-ray instrumentation have enabled *in-situ* and *in-operando* measurements of the microstructural and crystal structural changes in materials using multi-scale X-ray scattering techniques. One such technique involves combining ultra-small angle X-ray scattering (USAXS), small angle X-ray scattering (SAXS), and wide angle X-ray scattering (WAXS) characterization into a single set of measurements with one sample configuration [18–20]. In this study, we investigate the simultaneous microstructural and crystal structural changes in Na- and Ca-montmorillonites on heating to 1150 °C using USAXS/SAXS/WAXS measurements. USAXS, SAXS, and WAXS capture the clay morphology, the characteristic basal spacing, and the crystalline structures of clays collectively spanning a size range of μm to Å in one combined measurement. While the meso- and

* Corresponding author at: Department of Civil and Environmental Engineering, Princeton University, Princeton, NJ 08544, United States.
E-mail address: ge2131@caa.columbia.edu (G. Gadikota).

http://dx.doi.org/10.1016/j.fuel.2017.01.092
0016-2361/

nano-scale morphologies are determined using USAXS and SAXS, the structural changes are determined using WAXS.

While most natural clay-bearing geologic materials such as shales are modeled assuming a disordered fractal morphology [21–23], this is not always the case with clays. Clays have hierarchical structures with layered morphologies comprising interlayer nanopores, mesopores, and micropores associated with the arrangement of the clay units. We have modeled the layered, hierarchical morphologies from the combined USAXS/SAXS data, including changes in the surface areas, porosities, and size distributions specific to Na-montmorillonite and Ca-montmorillonite clays in the form of pelletized powder samples as they are heated to 1150 °C.

Na-montmorillonite and Ca-montmorillonite are swelling clays that have the characteristic ability to sorb variable amounts of water depending on the relative humidity of the environment [15,16,24]. This behavior is captured by changes in the interlayer basal distances that is found in the SAXS regime [25]. The zero and single-layer hydrates in smectites (a clay family that includes Ca- and Na-montmorillonites) give rise to basal distances corresponding to (9.5–10.2) Å and (11.6–12.7) Å, respectively [16,26–33]. While X-ray scattering and diffraction (XRD) studies report changes in basal distances on heating to <200 °C [17,25,34–45], changes in the basal distances on heating clays from ambient temperature to 1150 °C, measured together with the corresponding microstructural changes have not been reported to-date.

Here, we report the changes in the USAXS/SAXS/WAXS profiles of Na- and Ca-montmorillonites on heating to 1150 °C. The combined USAXS/SAXS data are modeled to obtain the pore size distributions associated with the hierarchical morphologies in pelletized clays, their surface areas and volume fractions. Interpretation of these results is correlated with observed changes in the characteristic interlayer peak, and also changes in characteristic montmorillonite phases, as well as formation of newer phases such as mullite ($2Al_2O_3{\cdot}SiO_2$) at elevated temperatures. Using multiple complementary techniques such as Brunauer–Emmett–Teller (BET) sorption and XRD in *ex-situ* measurements may produce similar results based on the analyses of heat-treated samples, but they do not provide insights into the hierarchical morphological changes in the materials. Specifically, this includes the temperature transitions at which major microstructural and structural events occur, including the collapse and appearance of new phases, changes in morphological ordering, and nuanced differences in the microstructure and structure of two clays having similar clay sheet arrangements but with variations in interlayer cation substitution (e.g., Na^+ *versus* Ca^{2+} within montmorillonite clay interlayers).

2. Materials and methods

Na-montmorillonite (SWy-3) and Ca-montmorillonite (STx-1) procured from The Source Clays Repositories[1] (Purdue University, West Lafayette, IN) are ground to a size smaller than 75 μm, and compacted into pellets. This approach is useful for understanding the incorporation of clay particles into natural and engineered composite materials. The thickness of each compacted pellet of Na- or Ca-montmorillonite is typically ≈ 0.5 mm. The heat treatment of the clays is performed by placing the pellet in a Linkam TS1500 heating stage (Linkam Scientific Instruments Ltd., Tadworth, UK) where the temperature control is to within ±0.1 °C. The temperature ramp rate is set to 2 °C/min (up to 4 °C/min over parts of the range away from obvious transitions), with starting and final temperatures of 30 °C and 1150 °C, respectively. The Linkam TS1500 stage is appropriately aligned for the synchrotron beamline experiments.

The multi-scale X-ray scattering experiments are performed at the USAXS instrument at sector 9-ID at the Advanced Photon Source (APS), Argonne National Laboratory, Argonne, IL. Using this instrument, USAXS measurements are combined with pinhole-camera based SAXS measurements and with WAXS measurements. The USAXS, SAXS and WAXS data comprise scattering or diffracted intensity, $I(q)$ *versus* q where $q = (4\pi/\lambda)\sin\theta$ and $q = (2\pi/d)$ to determine a lattice spacing, d, from an XRD peak in the WAXS data), λ is the X-ray wavelength and θ is half of the scattering or diffracted angle, 2θ. Data collection times for USAXS, SAXS and WAXS are 90 s, 30 s, and 30 s, respectively, for a total of ≈ 3 min, including time for instrument stage motions. Thus, all measurements are made within a few minutes of each other without changing the sample configuration within the beam, which greatly reduces any uncertainties arising from configuration changes.

A pair of high-resolution X-ray slits is used to define the beam size, which is set to (0.8 × 0.8) mm for USAXS and (0.2 × 0.2) mm for SAXS (pinhole SAXS or pin-SAXS) and WAXS. This latter setting allows the detector pixel size, (172 × 172) μm, for both SAXS and WAXS to be compatible with the incident beam collimation and flux. The sample-to-detector distances for SAXS and WAXS are set to 547 mm and 181 mm, respectively. The total X-ray flux at the sample is ≈ 10^{13} photon s^{-1}. The q values and sample-to-detector distances are calibrated using silver behenate and the NIST standard reference material, SRM 640d (Si). The X-ray λ = 0.59 Å (X-ray energy = 21.0 keV). Collected data are reduced and analyzed using the *Irena* [46] and *Nika* [47] software packages written in *IgorPro* (Wavemetrics, Lake Oswego, OR). Computed standard uncertainties in the reduced data are represented by vertical bars in the figures, and are typically ±5% of the mean, unless indicated otherwise. For the interlayer and other XRD peaks, the peak position fits can be determined to within a standard uncertainty in q that is always less than ±0.005 $Å^{-1}$, with a corresponding standard uncertainty in d-spacing less than ±0.01 Å.

3. Results

We discuss the changes observed in the USAXS, SAXS, and WAXS $I(q)$ as a function of q data as Na- and Ca-montmorillonite are heated, based on the effects of various temperature ranges on the key microstructural and structural features. The temperature ranges of interest identified are (i) (30–200) °C, (ii) (200–800) °C, (iii) (800–1000) °C, and (iv) (1000–1150) °C, which correspond to the removal of interlayer water, slow dehydroxylation, sintering, and then major morphological transitions from layered hierarchical to complex fractal structures, respectively.

The hierarchical morphology of the clays comprising the interlayer nanopores between adjacent clay sheets, mesopores between stacked clay sheets [48], and larger macropores between clay grains, correspond to identifiable q-ranges in the combined USAXS/SAXS regime as presented in Fig. 1. This is useful for reference in interpreting the USAXS/SAXS data in terms of the microstructural and structural changes in Na- and Ca-montmorillonite on heating, considered in detail in the following sections.

(i) 30–200 °C

The combined USAXS/SAXS data curves for Na- and Ca-montmorillonites on heating from 30 °C to 200 °C are presented in Figs. 2(a-1) and 3(a-1), respectively. The USAXS curves in the q range: (10^{-4} to 10^{-1}) $Å^{-1}$ correspond to a length scale regime of micrometers down to nanometers. The characteristic USAXS curves for Na-montmorillonite are smoother and more continuous

[1] Certain commercial materials, equipment and references are identified in this paper only to specify adequately experimental procedures. In no case does such identification imply recommendation by NIST nor does it imply that the material or equipment identified is necessarily the best available for this purpose.

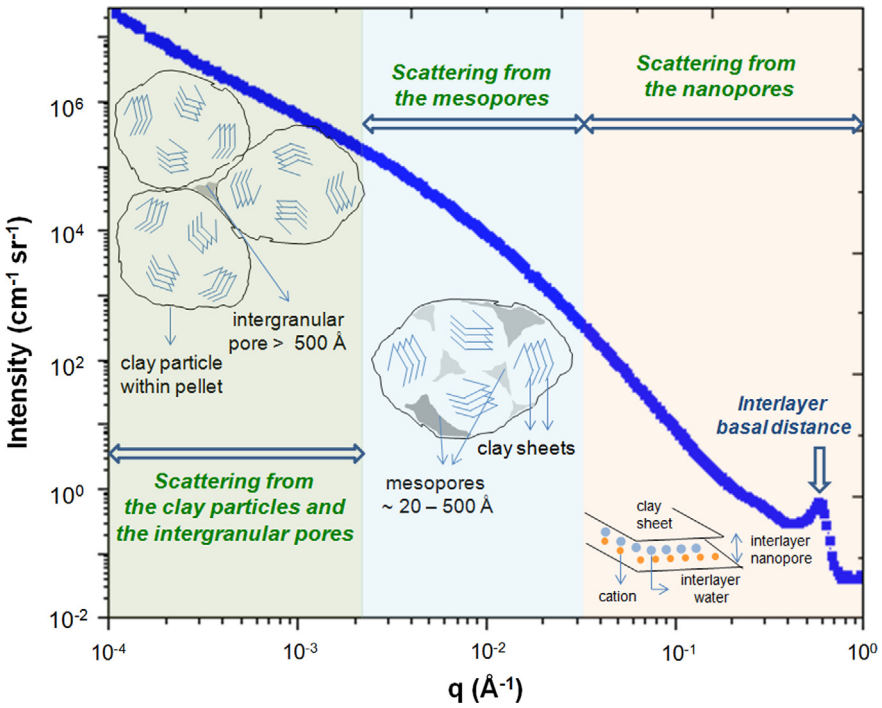

Fig. 1. Schematic representation of hierarchical morphologies in clay structures as modeled from combined USAXS/SAXS data. Data shown for Na-montmorillonite is at 26 °C. Vertical bars are computed standard deviations in measured USAXS/SAXS intensities.

compared to those for Ca-montmorillonite, where their slopes differ across three regions: (10^{-4} to 2.5×10^{-3}) $Å^{-1}$, (2.5×10^{-3} to 6.0×10^{-2}) $Å^{-1}$, and (6.0×10^{-2} to 1.5) $Å^{-1}$. The more distinct scattering slopes in Ca-montmorillonite *versus* the smoother and more continuous curves for Na-montmorillonite are indicative of more scale-separated, distinctive morphologies corresponding to the spatial regimes listed above, compared to a more disordered (perhaps more flexible) structure in Na-montmorillonite.

Changes in the intensity curves are greater in Na-montmorillonite compared to Ca-montmorillonite indicating that heat has a greater impact on less ordered clay structures (Table 1, Figs. 2(a-1) and 3(b-1)). These results also suggest that the changes at low q (coarse features) are smaller compared to those at high q (fine features). For clarity, data in the q range: (0.1–1.5) $Å^{-1}$ for Na- and Ca-montmorillonites are presented in Figs. 2(a-2) and 3(a-2), respectively.

Particularly significant changes in the scattering behaviors of Na- and Ca-montmorillonite are evident in the q range: (0.1–1.5) $Å^{-1}$. The distinct small angle diffraction peaks in Na- and Ca-montmorillonite, corresponding to 0.58 $Å^{-1}$ and 0.53 $Å^{-1}$, represent the clay (001) basal spacings (Figs. 2(b-1) and 3(b-1)). These basal spacings in Na- and Ca-montmorillonite are 10.8 Å at 26 °C and 11.8 Å at 30 °C, respectively. Zero (0 W) and single-layer (1 W) hydrates of smectites have reported basal spacings of (9.5–10.2) Å and (11.6–12.7) Å, respectively [16,26–30]. It can be inferred that the hydrated states of the smectites bearing Na-montmorillonite and Ca-montmorillonite at the start of these experiments are 0–1 W and 1 W, respectively.

Changes in the Na-montmorillonite basal spacing are smaller than for Ca-montmorillonite as water is removed on heating to 200 °C. The basal distances of Na-montmorillonite at (26, 105 and 200) °C are (10.77, 9.99 and 9.78) Å, respectively, while those of Ca-montmorillonite at (30, 105 and 197) °C are (11.74, 10.84 and 9.91) Å, respectively. (The basal distance of 9.91 Å in Ca-montmorillonite is unchanged at 179 °C (shown in Fig. 3) and 197 °C). The basal distances at ≈ 200 °C for both Na-montmorillonite and Ca-montmorillonite correspond to those of zero-layer hydrates of the montmorillonites [16,26–33]. Our studies are in agreement with previously published results indicating the transition of the basal distance from the 1 W to 0 W states is not complete at 125 °C in Ca-montmorillonite [16], and heating in excess of 130 °C is required for the complete removal of interlayer water. A distinct reduction in the intensity of the characteristic swelling peak in Ca-montmorillonite compared to Na-montmorillonite on heating is also noted (Figs. 2(a-2) and 3(a-2)).

In addition to the changes in the characteristic basal spacing, the changes in the crystal structure of Na-montmorillonite and Ca-montmorillonite can be obtained from the WAXS data. While various peaks can be analyzed to determine the structural changes on heating, two peaks that typify changes on heating correspond to: q = 4.135 $Å^{-1}$ with d-spacing = 1.52 Å for the combined (026) and (135) montmorillonite diffraction peaks in Na-montmorillonite; and q = 1.405 $Å^{-1}$ with d-spacing = 4.47 Å for the (110) montmorillonite diffraction peak in Ca-montmorillonite (Fig. 4(a-1) and (b-1)). Both peaks are characteristic of montmorillonite structures as reported in several studies [34,49,50]. Because of this, the choice of either characteristic peak is not expected to yield significantly different analyses. On heating from ambient temperature to 200 °C, a small expansion in the crystal structure is noted from the decrease in q of the peak positions in Na- and Ca-montmorillonite (Fig. 4(a-1) and (b-1)).

We note that clays are not perfectly crystalline materials and the turbostratic ordering in the clay sheets result in many broad peaks rather than sharper and more distinct peaks [51–53]. The characteristic peak that best represents the turbostratic ordering of clays, the so-called h-k bend, is found at a q-value between 2.35 $Å^{-1}$ and 2.65 $Å^{-1}$ in Na- and Ca-montmorillonite, as shown in Fig. 5(a-1) and (b-1), respectively. Significant changes in the h-k bend are not evident on heating the clays from ambient temperature to 200 °C, indicating that the quasi-crystallinity of these clays is not directly influenced on heating in this temperature range.

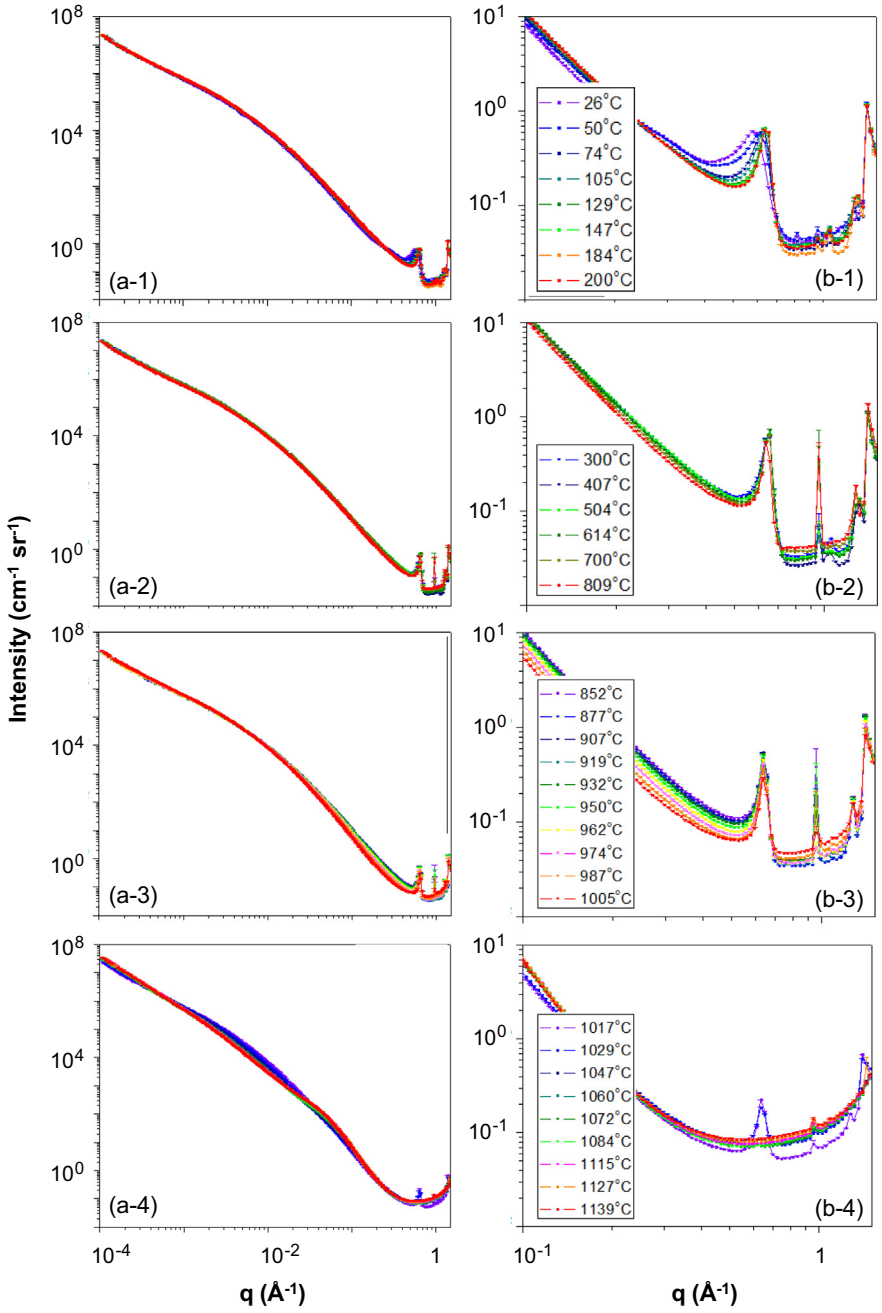

Fig. 2. Changes in combined USAXS/SAXS data for Na-montmorillonite in temperature ranges: (30–200) °C (a-1); (200–800) °C (a-2); (800–1000) °C (a-3); and (1000–1150) °C (a-4). Changes in SAXS data for the basal distance diffraction peaks are magnified in (b-1), (b-2), (b-3) and (b-4). Vertical bars are computed standard deviations in measured USAXS/SAXS intensities.

(ii) 200–800 °C

Combined USAXS/SAXS curves for Na- and Ca-montmorillonites on heating from 200 °C to 800 °C are presented in Figs. 2(a-2) and 3 (a-2), respectively. The data curves at 300 °C remain similar to those measured at 200 °C for Na-montmorillonite and 179 °C for Ca-montmorillonite. Reductions in the scattering intensities are noted across the entire q range in both montmorillonites on heating from 300 °C to 817 °C (Table 1). These results suggest that the overall morphologies associated with $q < 10^{-3}$ Å^{-1} do not vary significantly. Similarly, the nano-scale morphologies do not exhibit as significant a variation in this temperature range compared to heating from 30 °C to 200 °C (Figs. 2(b-2) and 3(b-2)).

The changes in the basal distances in Na- and Ca-montmorillonite that correspond to the small-angle diffraction peaks within the q ranges (0.5–0.7) Å^{-1} are not as pronounced as found in the lower temperature range. However, unlike for Na-montmorillonite, the interlayer peak intensity for Ca-montmorillonite continues to decrease with increasing temperature to 800 °C. Meanwhile, the basal distances of Na- and Ca-montmorillonite are ≈ 9.8 Å throughout this temperature range (Figs. 2(b-2) and 3(b-2)).

Unlike the subtle trends seen in the USAXS/SAXS data, significant changes in crystal structure are evident on heating from 600 °C to 800 °C in both Na- and Ca-montmorillonite dare consistent with

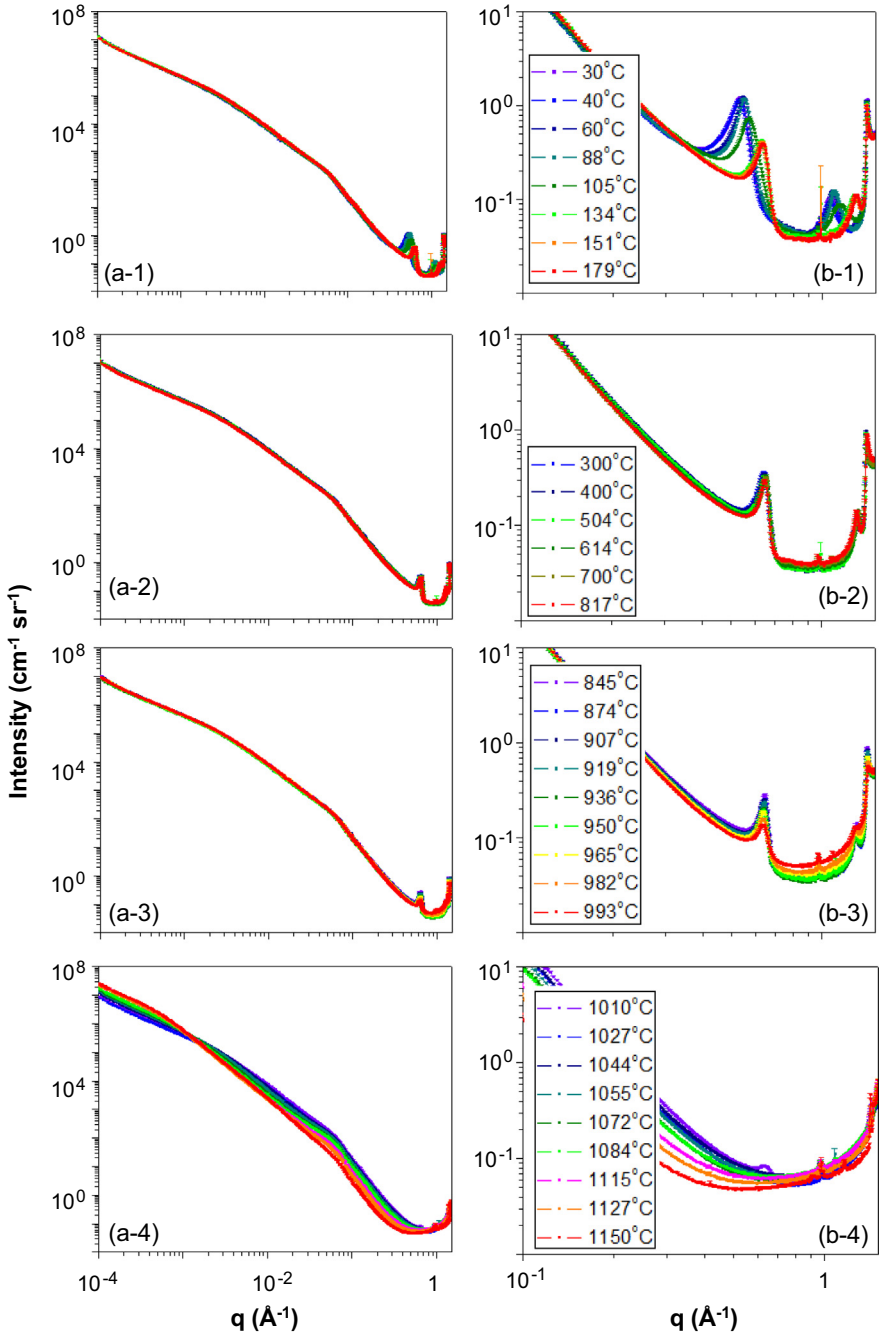

Fig. 3. Changes in combined USAXS/SAXS data for Ca-montmorillonite in temperature ranges: (30–200) °C (a-1); (200–800) °C (a-2); (800–1000) °C (a-3); and (1000–1150) °C (a-4). Changes in SAXS data for the basal distance diffraction peaks are magnified in (b-1), (b-2), (b-3) and (b-4). Vertical bars are computed standard deviations in measured USAXS/SAXS intensities.

reported findings that the collapse of the montmorillonite lattice begins at 600 °C [54]. In Ca-montmorillonite, increases in temperature shift the selected (1 1 0) diffraction peak towards larger q, indicating a smaller d-spacing. The changes in the characteristic Na- and Ca-montmorillonite diffraction curves in Fig. 4(a-2) and (b-2) are also consistent with the observed changes in the h-k bend at $q \approx 2.5$ Å^{-1} that reflects the turbostratic ordering of clays (Fig. 5 (a-2) and (b-2)), which is indicative of the dehydroxylation of the montmorillonite lattice [54].

(iii) 800–1000 °C

In this range, changes in the shapes of the USAXS curves are more prominent in Na-montmorillonite than in Ca-montmorillonite. A significant decrease in SAXS intensity of Na-montmorillonite is noted at $q \approx 0.1$ Å^{-1} (Table 1) indicating that the nano-scale morphology is altered in this temperature range. In Na-montmorillonite, the data curve steepens in the q regime range: (10^{-2} to 10^{-1}) Å^{-1} on heating, and the intensity decreases in this range. In the SAXS regime, an increase in temperature from 800 °C to 1000 °C reduces the intensities but does not change the positions of the interlayer peaks which remain at a q of ≈ 0.64 Å^{-1} in both Na- and Ca-montmorillonite (Figs. 2(b-3) and 3(b-3)). The peak intensities of the basal distance (0 0 1) peaks in Na- and Ca-montmorillonite at 993 °C are (61 and 48)% of the peak intensities at 845 °C, which suggests that the dehydroxylation of the montmorillonites on heating reduces the intensities of the

Table 1
Intensity changes in USAXS/SAXS data at $q = (10^{-3}, 10^{-2}$ and $10^{-1})$ Å^{-1} on heating. % changeinintensity $= 100 \times \frac{I(T_2)-I(T_1)}{I(T_1)}$ where $I(T_1)$ is intensity at temperature, T_1, and $I(T_2)$ is intensity at temperature, T_2.

Na-montmorillonite		Ca-montmorillonite	
On heating from T_1 (°C) to T_2 (°C)	% change observed in q	On heating from T_1 (°C) to T_2 (°C)	% change observed in q
26–200	12% at 10^{-3} Å^{-1} 16% at 10^{-2} Å^{-1} 26% at 10^{-1} Å^{-1}	30–179	9% at 10^{-3} Å^{-1} 12% at 10^{-2} Å^{-1} 13% at 10^{-1} Å^{-1}
300–809	−12% at 10^{-3} Å^{-1} −13% at 10^{-2} Å^{-1} −8% at 10^{-1} Å^{-1}	300–809	−12% at 10^{-3} Å^{-1} −7% at 10^{-2} Å^{-1} −4% at 10^{-1} Å^{-1}
852–1005	3% at 10^{-3} Å^{-1} −9% at 10^{-2} Å^{-1} −52% at 10^{-1} Å^{-1}	845–993	3% at 10^{-3} Å^{-1} 2% at 10^{-2} Å^{-1} −10% at 10^{-1} Å^{-1}
1010–1150	−22% at 10^{-3} Å^{-1} −56% at 10^{-2} Å^{-1} 60% at 10^{-1} Å^{-1}	1010–1150	39% at 10^{-3} Å^{-1} −67% at 10^{-2} Å^{-1} −83% at 10^{-1} Å^{-1}

interlayer peaks. Other significant changes in the crystal structure are evident in both Na- and Ca-montmorillonite in this temperature range. The intensities of the characteristic peaks, as well as those of the h-k bend in both Na- and Ca-montmorillonite, are progressively reduced on heating. This is indicative of the ongoing disruption of the turbostratic structure of the clays (Figs. 4(a-3), (b-3), 5(a-3), and (b-3)).

(iv) 1000–1150 °C

Significant morphological transitions are evident on heating Na- and Ca-montmorillonite from 1000 °C to 1150 °C (Figs. 2(a-4), (b-4) and 3(a-4), (b-4)). The changes are greater in Na-montmorillonite than in Ca-montmorillonite (Table 1). At $q < 5 \times 10^{-4}$ Å^{-1}, the scattering intensities in Na-montmorillonite increase on heating from 1000 °C to 1150 °C. In the q-range: $(5 \times 10^{-4}$ to $2 \times 10^{-2})$ Å^{-1}, the scattering intensities decrease but the gradient in the scattering curve becomes steeper. The hierarchical size distribution model used at lower temperatures starts to break down and fails to give results for 4 discrete pore populations. The changes in the size distributions towards a fractal morphology of the clay pellets are consistent with the phase transitions and enhanced sintering effects at temperatures in excess of 1000 °C (Table 1) [58]. The characteristic small-angle diffraction peak at $q = 0.65$ Å^{-1} that corresponds to the basal (001) distance disappears on heating above 1029 °C, indicating a complete collapse at these temperatures of the original structure of Na-montmorillonite with regular basal interlayer distances. In Ca-montmorillonite, the scattering intensities decrease on heating through this temperature range for $q > 1.5 \times 10^{-3}$ Å^{-1}, but increase for $q > 10^{-3}$ Å^{-1}. These changes are indicative of densification with reduced internal nano-porosity. Also, the basal distance peak in Ca-montmorillonite disappears on heating above 1010 °C (Figs. 2(b-4) and 3(b-4)), a slightly lower temperature than for Na-montmorillonite.

The changes in the microstructure and structure of Na-montmorillonite and Ca-montmorillonite in this temperature regime are correlated with the complete disappearance of the characteristic basal (001) diffraction peaks arising from the interlayers (Fig. 4(a-4) and (b-4)). Indeed, the turbostratic structure of Na-montmorillonite disappears on heating at these temperatures, and is replaced by the onset of diffraction peaks characteristic of mullite [55,56] at 2.46 Å^{-1} (d-spacing = 2.55 Å) and cristobalite (SiO_2) at 2.53 Å^{-1} (d-spacing = 2.48 Å) [57] (Fig. 5(a-4)). In Ca-montmorillonite, the adjacent development of mullite and cristobalite peaks is consistent with previously published studies (Fig. 5(b-4)) [58]. The small differences in the peak sizes of mullite are attributed to the variable forms of mullite that can be formed at varying temperatures. The representative chemical formula for mullite is: $Al_{(4+2x)}Si_{(2-2x)}O_{(10-x)}$ where x varies from 0.2 and 0.9, depending on temperature [59,60].

4. Discussion

The detailed microstructural features of Na- and Ca-montmorillonite on heating are ascertained from the USAXS/SAXS curves presented in Figs. 2 and 3. These analyses are complimented by the structural changes in the WAXS regime (Figs. 4 and 5). In this section, we interpret the USAXS/SAXS/WAXS data presented in the previous section to offer insights into the combined microstructural and structural changes in clays. The morphological changes of Na- and Ca-montmorillonite on heating are interpreted in Section 4.1. The changes in the basal distances and the intensity of the small angle diffraction peak in Na-montmorillonite and Ca-montmorillonite are discussed in Section 4.2. The changes in the characteristic Na-montmorillonite and Ca-montmorillonite diffraction peaks in the WAXS regime are discussed in Section 4.3.

4.1. Morphological perspective

The key morphological features of clays, such as the diameters or volume fractions, porosities, and surface areas of the scattering features, can be determined from the combined USAXS/SAXS intensity curves presented in Figs. 2 and 3 by the appropriate application of well-known small-angle scattering functions and models [61–70]. Regardless of the model used, it should be noted that the scattering as a function of q is related to the Fourier transform of the real-space electron density distribution. This means that coarse features give rise to the scattering at low q while nano-scale features give rise to the scattering at high q. In the present case, for much of the temperature range of interest (30–1000 °C), all scattering features were assumed to be oblate pores or voids with an aspect ratio of 0.2, which is consistent with the platelet-like morphology of clays based on TEM investigations [48]. The scattering is assumed to arise from voids because the samples comprise pressed powdered clay pellets that are solid clay material except for the various hierarchical pore morphologies. The calibrated scattering intensity from the ith pore population, $I_i(q)$, normalized to the incident X-ray flux and sample volume, is proportional to its overall volume fraction normalized to the total sample volume, Φ_{Vi}, and the mean volume of its individual pores, V_{Pi} (at low and intermediate q), to its surface area per unit sample volume, S_{Vi} (at high q), and to the scattering contrast factor, $|\Delta\rho|^2$. The latter is the square of the difference in scattering length density (SLD or ρ) between inside the pores (H_2O or void) and outside in the solid clay phase (determined by density and chemical composition, and dependent upon the degree of dehydroxylation). Knowledge of the correct contrast factor, $|\Delta\rho|^2$, is essential for calculating either true volume fractions or surface areas per unit sample volume, but the term cancels out when determining the surface area per unit volume of scattering features, themselves.

In our case, we used an entropy maximization technique, *MaxEnt* [64], to optimize contributions to the scattering intensity from a pre-defined set of histogram bin sizes for scattering features of a given shape. While this approach requires many iterations for the model to converge, [64,65], it also allows us to represent the hierarchical morphologies of complex materials such as clays. In this study, we identify from the MaxEnt size distributions derived from the scattering curves 4 void populations within the

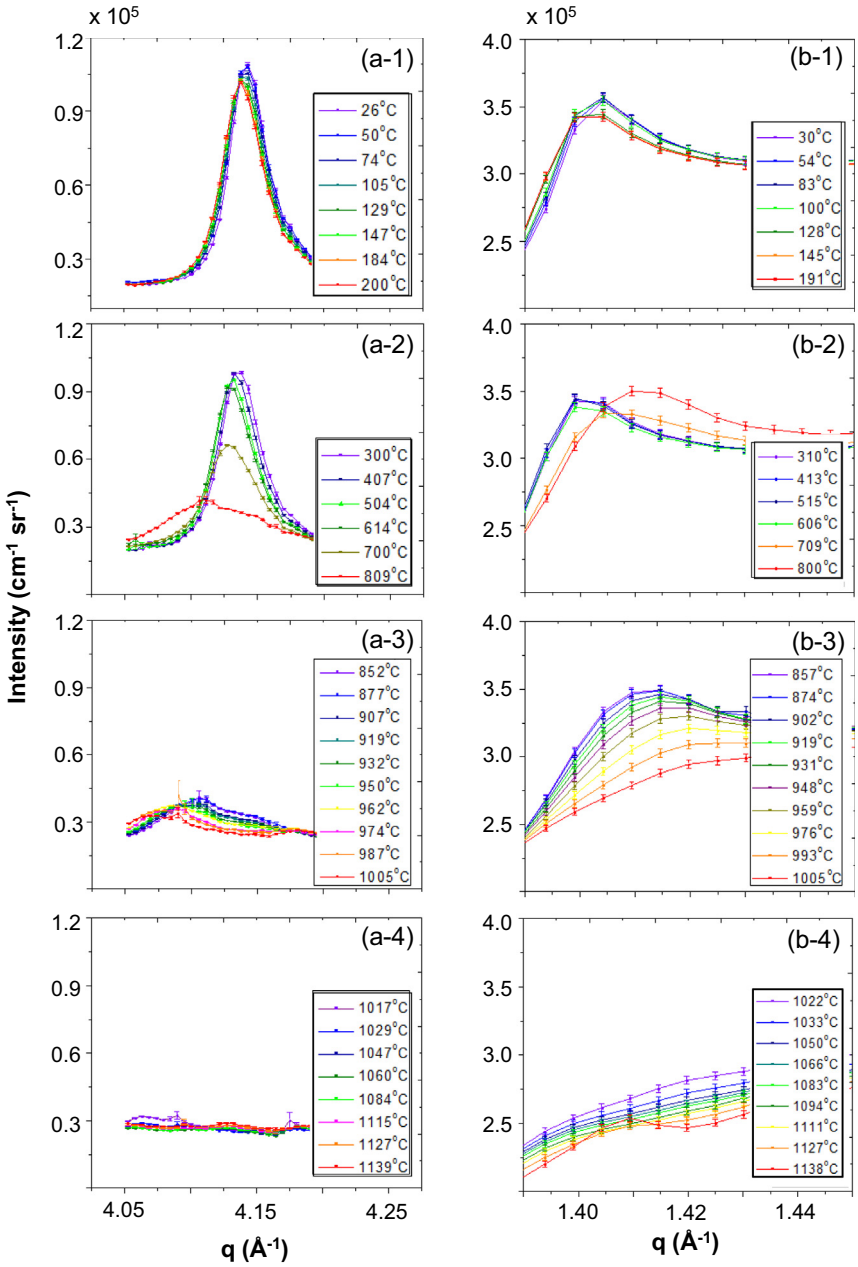

Fig. 4. Changes in the characteristic diffraction peak in (a) Na-montmorillonite and (b) Ca-montmorillonite in temperature ranges: (30–200) °C ((a-1), (b-1)); (200–800) °C ((a-2), (b-2)); (800–1000) °C ((a-3), (b-3)); and (1000–1150) °C ((a-4), (b-4)). Vertical bars are computed standard deviations in measured WAXS intensities.

microstructures of Na- and Ca-montmorillonite. Our assumption that the voids are oblate spheroids with aspect ratio, $\beta = 0.2$, accounts for the platelet like morphology of clays [48]. We use this approach to follow the morphologies of the clays as they dynamically change with temperature up to 1000 °C, as evident in Figs. 2 and 3. More details of the pore size distribution analysis, including the basis of the maximum entropy method, and how the 4 pore populations are identified, are provided in the Supporting Information.

Above 1000 °C, the hierarchical pore population model breaks down and the scattering becomes indicative of a disordered, fractal morphology, which is consistent with the enhanced sintering and phase transitions that occur at these temperatures [58]. Thus, in this high-temperature regime, we assume volume- and surface-fractal morphologies with non-integral scaling components, D_V and D_S, respectively [66–70]. Apart from the non-integral scaling exponents, volume- and surface-fractal morphologies can be characterized by building-block sizes (finest pore elements in the current context), correlation lengths, ξ_V and ξ_S, beyond which fractal scaling breaks down. Volume-fractals are also characterized by the volume fraction of the features, Φ_V (here pores) and can also provide an estimate for the fraction of sample characterized by the overall volume-fractal morphology. Surface-fractals are further characterized by a smooth surface area, S_O, associated with the coarse morphology without taking into account surface roughness, and also the fully rough surface area, S_{SF}, taking all roughness into account. In our case we associate the fractal morphologies with the residual porous features that persist during the high-temperature transformations from clay to mullite phases, and the progressive sintering of the overall morphologies that occur in parallel with these transformations. More details of the fractal models assumed are provided in the Supporting Information.

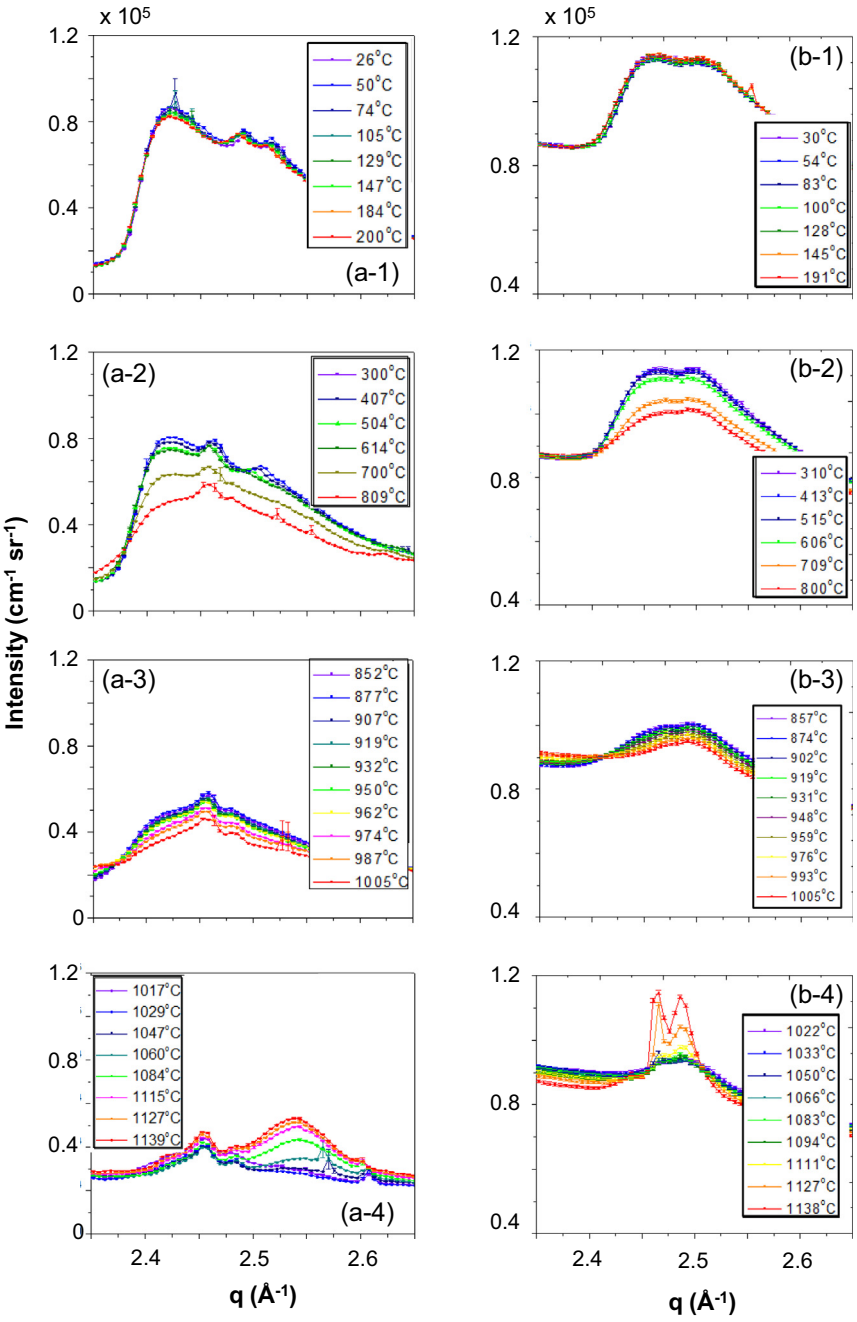

Fig. 5. Changes in the characteristic h-k bend in (a) Na-montmorillonite and (b) Ca-montmorillonite in the temperature ranges: (30–200) °C ((a-1), (b-1)); (200–800) °C ((a-2), (b-2)); (800–1000) °C ((a-3), (b-3)); and (1000–1150) °C ((a-4), (b-4)). Vertical bars are computed standard deviations in measured WAXS intensities.

4.1.1. Development of a representative micro- and nano-structural model for the heat treatment of Na- and Ca-montmorillonite

A key input for determining changes in the microstructure from the USAXS curves is an appropriate contrast factor. We calculated the contrast factor (which is a function of the chemical composition and density of the phases within the sample materials) using the *Irena* analysis package [46]. In this study, the chemical compositions of Na- and Ca-montmorillonite change dynamically with temperature. The key thermo-chemical events during the heating of Na- and Ca-montmorillonite are the removal of water which occurs on heating to 200 °C, the gradual dehydroxylation of montmorillonite which occurs between 300 °C and 800 °C, the progressive conversion to mullite starting above 800 °C, and the complete loss of the montmorillonite structure on heating beyond 1050 °C. The contrast factors used in this study are represented in Fig. 6.

Associated with determining the appropriate contrast factors for the various temperature ranges of interest, is the need to identify the different void populations indicated in the *MaxEnt* size distribution analysis. Four distinct populations in Na-montmorillonite and Ca-montmorillonite can be identified in the size distributions for these pelletized clays. The first (finest) population represents the nanoporosity (<20 Å diameter, <4 Å in thickness dimension), while the second and the third populations represent the mesopores in the clay microstructure (20–500 Å). The fourth (coarsest) population is indicative of scattering that arises from the grains and intergranular spacings in clays (> 500 Å) (Fig. 7).

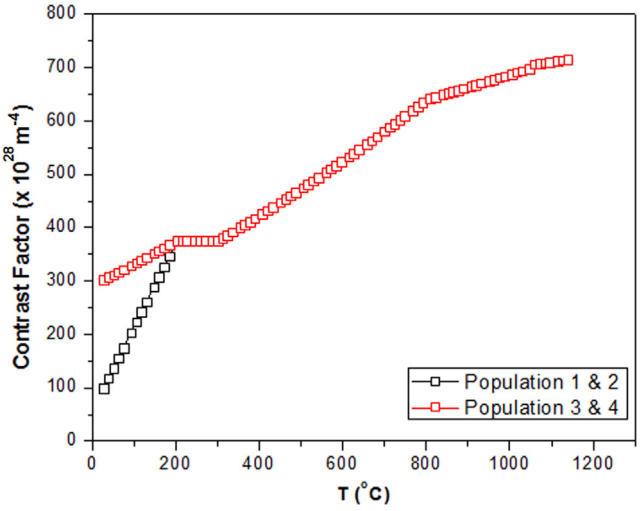

Fig. 6. Calculated contrast factors assumed as a function of temperature for determining microstructural properties of Na-montmorillonite and Ca-montmorillonite.

We attribute the first population (1) to the interlayer nanopores between clay layers. On heating to 200 °C, the water in the clay interlayer pores is gradually removed. Any water residing in the small mesopores represented by the second population (2) is also removed on heating to 200 °C. Therefore, varying contrasts are calculated for populations 1 and 2 between the temperatures of 30 °C and 200 °C as the interlayer water is removed. The scattering length density (SLD) of the solid clay structure is calculated to be 19.37×10^{14} m^{-2} based on a density of 2.3 g/cm^3 and the chemical composition of Na- and Ca-montmorillonite under ambient conditions. Meanwhile, the SLD for H_2O is 9.42×10^{14} m^{-2}.

In the absence of other information, we made a simple assumption that the fraction of water-filled pore interface with solid decreases linearly from 100% to 0% over this temperature range. This implies that the scattering contrast factor (the square of the SLD difference) increases linearly with temperature from that for clay/H_2O: 99.0×10^{28} m^{-4} at ambient to that for clay/air: 375.2×10^{28} m^{-4} at 200 °C, as the water is removed for populations 1 and 2. We assume that void populations 3 and 4 are essentially air-filled from the outset, but the contrast factor is between air (essentially zero) and the clay, which at these length scales contains the associated interlayer and nanoscale water assumed to be present at the given temperature. In this case, our assumptions imply that the "solid" SLD increases linearly from 17.38×10^{14} m^{-2} to 19.37×10^{14} m^{-2} in populations 3 and 4 on heating to 200 °C, and the contrast factors are the square of these SLDs. Once the interlayer water is removed at 200 °C, the contrast for all populations with air is 375.2×10^{28} m^{-4} (Fig. 6).

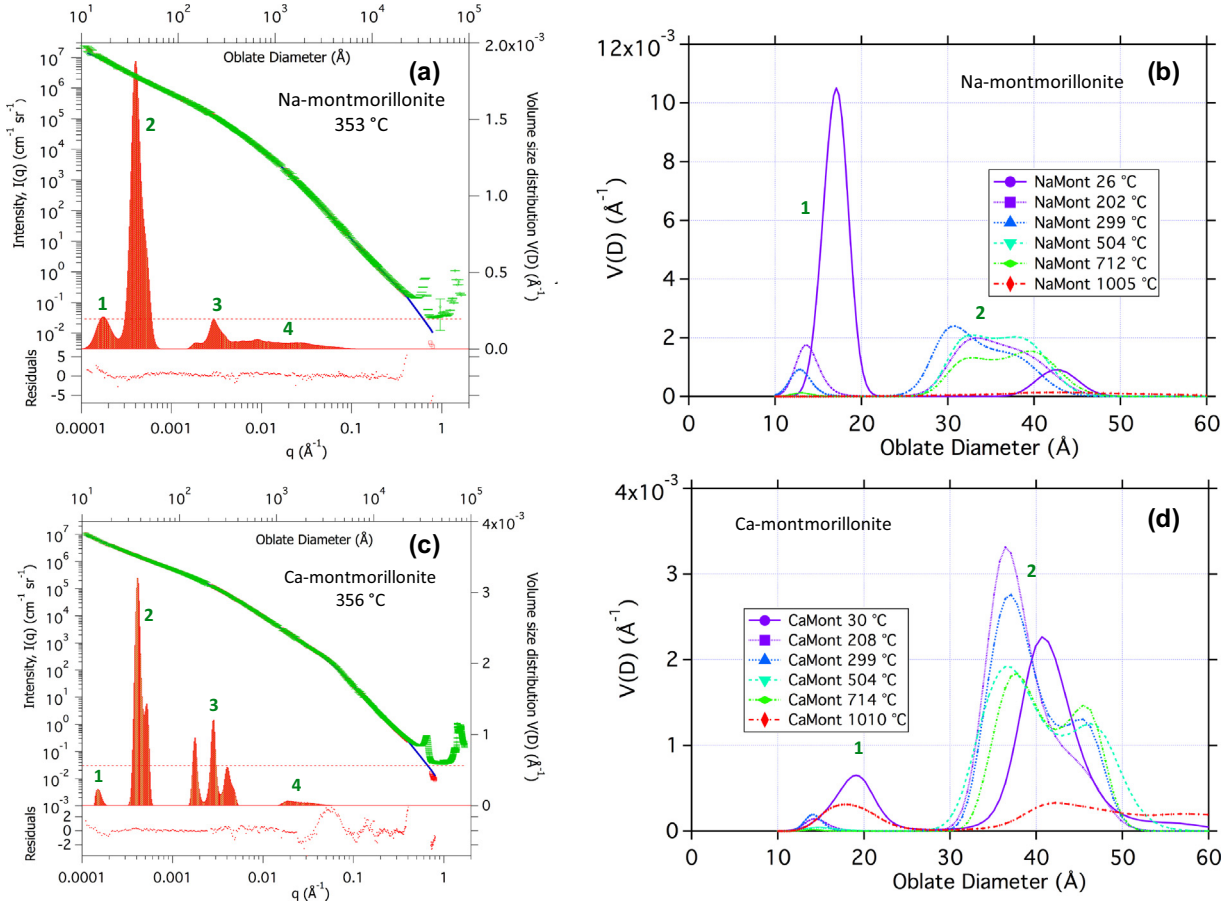

Fig. 7. Typical MaxEnt volume fraction size distributions with fits to data, together with plots showing fine populations 1 and 2 pore size distributions at selected temperatures up to ≈ 1000 °C for (a, b) Na-montmorillonite, and (c, d) Ca-montmorillonite. All pores assumed to have 0.2 aspect ratio. Size distributions are with respect to unit increment in oblate (large) pore diameter. Panels (a) & (b) show MaxEnt fits to combined USAXS/SAXS data, excluding the basal interlayer peak & other small-angle diffraction peaks. Size distributions are plotted on a linear-log scale to show all 4 populations. Note actual integrated volume fractions of populations 3 & 4 are significantly larger than for 1 & 2. In the hierarchical structure of montmorillonite, populations 1, 2 & 3 represent pore size distributions with oblate pore diameters in the ranges: (10–25) Å, (30–50) Å & (150–400) Å, respectively, while population 4 represents voids associated with intergranular spacings > 500 Å within the pressed samples. Vertical bars represent computed standard uncertainties for measured USAXS/SAXS intensities. Estimated size distribution uncertainties are ±10%.

On heating from 200 °C to 800 °C dehydroxylation of montmorillonite occurs progressively. We made a simple assumption that the SLD changes linearly from 19.37×10^{14} m^{-2} (clay composition includes hydroxyl groups) to 25.29×10^{14} m^{-2} (which corresponds to the removal of hydroxyl groups), which implies that the contrast factor with air changes quadratically from 375.2×10^{28} m^{-4} (300 °C) to 639.6×10^{28} m^{-4} (800 °C). On heating beyond 800 °C, the progressive conversion to mullite is observed. The complete loss of the montmorillonite phase is evident at 1050 °C. Again, we approximate the gradual changes in the structure from montmorillonite to mullite by a simple linear increase in the contrast from 639.6×10^{28} m^{-4} at 800 °C to 698.6×10^{28} m^{-4} at 1050 °C. As the mullite phases develop beyond 1000 °C, the SLD changes linearly from 26.43×10^{14} m^{-2} at 1000 °C to 26.77×10^{14} m^{-2} at 1150 °C, and the contrast factor therefore increases quadratically to 716.7×10^{28} m^{-4}. The changes in scattering contrast factor with temperature are presented in Fig. 6 for all 4 void populations. These scattering contrast changes are accompanied by detailed morphological changes in Na- and Ca-montmorillonite on heating, as described below.

4.1.2. Micro- and nano-structural changes in Na- and Ca-montmorillonite on heating from ambient conditions to 1000 °C

We recall that the pores both within and between the clay sheets and stacks are modeled as oblate spheroids with an aspect ratio of 0.2 to represent the platelet-like morphology [48] of clays. The hierarchical morphology is represented by the nano-scale population 1and meso-scale populations 2 and 3. The voids associated with inter-granular spacings are represented by population 4. Populations 1, 2 and 3 represent the intrinsic pore sizes of the Na- and Ca-montmorillonites, while population 4 is essentially a measure of the coarseness of the samples together with the degree of packing of the powder grains in the pressed samples studied. This morphology is for the specific case of a Na- or Ca-montmorillonite powder compacted into a pellet. Meanwhile, based on our microstructural analyses (which are extensively discussed in the supplementary section), the $\beta = 0.2$ aspect ratio reasonably captures the non-spherical, semi-lamellar morphology of clays.

Typical *MaxEnt* size distributions derived from combined USAXS/SAXS data for Na- and Ca-montmorillonite are shown in Fig. 7, with the 4 pore populations indicated. Above 1000 °C the morphology progressively transforms heterogeneously into (ultimately) a mullite phase. In this regime the hierarchical pore population model breaks down and the residual void morphology is better modeled using the fractal approach, as previously indicated.

As a function of temperature, the *MaxEnt* size distributions have been analyzed to extract, for each of the populations 1 to 4, the mean oblate diameter, the population total volume fraction, and the population total surface area (Fig. 8). The nano- and meso-scale pore size diameters that represent populations 1 and 2, respectively, are presented in Fig. 8(a). The larger meso-scale pore size diameters and the voids associated with intergranular spacings that represent populations 3 and 4 are shown in Fig. 8(b). The nano-scale oblate pore diameters of population 1 are smaller than 20 Å in both Na- and Ca-montmorillonite, implying a mean opening dimension of the swellable interlayer of 3–4 Å. The small dimension is consistent with the interlayer spacings in 1–0 W Na-montmorillonite. However, these nano-scale pore populations (Figs. 7 and 8) are inclusive but not limited to the interlayer nanopores.

As the temperatures increase to 200 °C, the decrease in the size of the small dimension by 1–2 Å is consistent with the reduction in the interlayer space in Na- and Ca-montmorillonite on heating. On heating from 200 °C to 950 °C, these nanopore mean oblate diameters in Na and Ca-montmorillonite remain in the range of (12–14) Å, and (14–16) Å, respectively (Fig. 8(a)). Thus, the dehydroxylation of Na- and Ca-montmorillonite in the temperature range: 200–950 °C, does not, itself, appear to produce further significant changes in the sizes of the nanopores (or their opening dimensions).

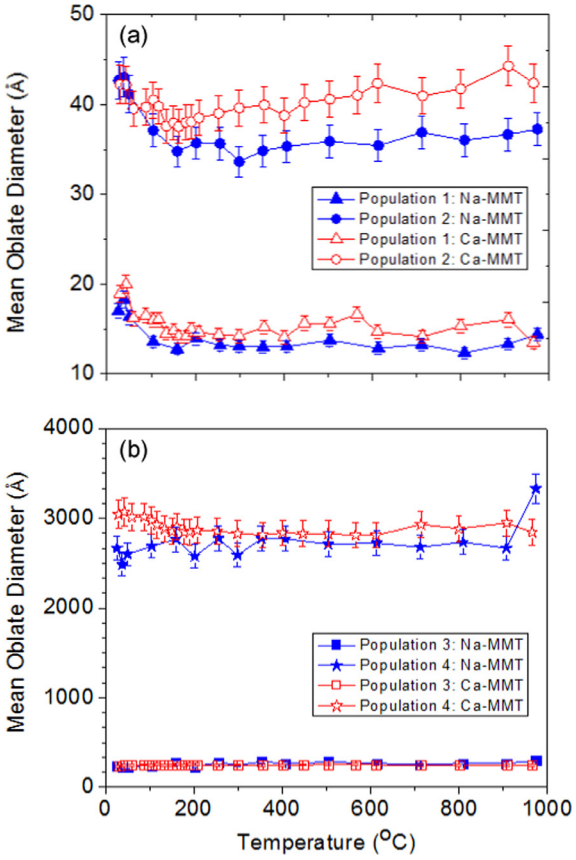

Fig. 8. Mean oblate diameters of pore populations in Na-montmorillonite and Ca-montmorillonite: (a) populations 1 & 2; (b) populations 3 & 4, on heating from 30 °C to 1000 °C. Vertical bars represent estimated standard deviation uncertainties.

On heating from ambient to 200 °C, a decrease in the size of the mesopores represented by population 2 is apparent (Fig. 8(a)). The mean oblate diameter for population 2 decreases from 45 Å to 36 Å or 38 Å on heating Na-montmorillonite or Ca-montmorillonite from 30 °C to 200 °C, respectively. The mean opening dimensions of these mesopores correspondingly decreases from 6 Å to <5 Å or ≈ 5 Å for Na- or Ca-montmorillonite, respectively. This reduction is likely associated with some shrinkage in the local clay morphology as water is removed from the fine population 1 pores. In the temperature range 200 °C to 950 °C, the mean oblate diameter of the population 2 mesopores slightly increases again to ≈ 38 Å and ≈ 42 Å for Na- and Ca-montmorillonite, respectively. This may be a result of some true densification of the clay solids during dehydroxylation – leaving larger pore spaces between the clay stacks. An increase in the temperature from 30 °C to 1000 °C does not impact the size of the larger population 3 mesopores in either Na- or Ca-montmorillonite, as shown in Fig. 8(b).

Indeed, this coarser level of porosity within the internal clay structure hierarchy remains remarkably constant in size with temperature. The population 4 size distribution, which is representative of the intergranular spacing within the pressed sample compacts, is expected to exhibit an oblate diameter size distribution that approximates to the more globular grain diameter size distribution of the crushed clay powder. Once again, these pores are slightly larger in Ca-montmorillonite than in Na-

montmorillonite. In the temperature range 30 °C to 200 °C, there is no systematic temperature dependence of their mean oblate diameter in Na-montmorillonite. In Ca-montmorillonite, heating decreases the population 4 mean oblate diameter from 3100 Å at 40 °C to 2850 Å at 200 °C. For temperatures exceeding 200 °C, the mean oblate diameters for population 4 in Na-montmorillonite and in Ca-montmorillonite range from 2600 Å to 2900 Å, and from 2700 Å to 3200 Å, respectively. Previous studies using transmission electron microscopy techniques show that the sizes of clay particles range from 2000 Å to 4000 Å [48,71,72] which is consistent with our findings.

In addition to the size distributions, the changes in the volume fractions of the intrinsic void spaces in Na- and Ca-montmorillonite provide insights into the overall morphological changes. Fig. 9(a) and (b) present changes in the intrinsic volume fractions of populations 1, 2, and 3, together with their total intrinsic porosity in Na-montmorillonite, and Ca-montmorillonite, respectively. These intrinsic component and total porosities are normalized to the true material sample volume with population 4 subtracted out, since this is simply pore space left over from less than 100% packing of the powder grains on pressing. Renormalized in this way, populations 1, 2 & 3 capture the morphology intrinsic to the pelletized clay morphology. At ambient temperature, population 1 which corresponds to the nanoscale porosity accounts for 84% of the overall void fraction in Na-montmorillonite (Fig. 9(a)). In contrast, population 1 only accounts for 8% of the overall porosity in Ca-montmorillonite (Fig. 9(b)). The significant reductions in porosity observed with increasing temperature are consistent with the sintering behavior of clays at elevated temperatures [3].

In Na-montmorillonite, the nano-scale porosity, which is represented by population 1, accounts for a significant part of the void fraction on heating from ambient temperature to 100 °C. In Ca-montmorillonite however, the meso-scale porosities represented by populations 2 and 3 account for a significant fraction of the void fraction within the same temperature range. The population 1 porosity is reduced to a very small fraction on heating beyond 300 °C in Na-montmorillonite and beyond 200 °C in Ca-montmorillonite. Despite the reduction in porosity for pores with oblate diameter <20 Å, the characteristic basal (001) diffraction peak (Figs. 2(b) and 3(b)) does not disappear even on heating to above 1000 °C, which indicates that the layered structure is maintained despite a reduction in the intensity of the nano-scale pores. The population 2 pore volume fraction of Na-montmorillonite decreases from 0.03 at 200 °C to 0.01 at 900 °C, while that for population 3 decreases from 0.03 at 200 °C to 0.02 at 900 °C. In Ca-montmorillonite the population 2 void fraction decreases from 0.03 to 0.002 over the temperature range from 200 °C to 900 °C while the population 3 void fraction persists even on heating to 1000 °C, decreasing from 0.12 to 0.05.

The changes in the intrinsic surface areas (Fig. 10(a) and (b)) follow similar trends to those for the intrinsic void fractions. As with the intrinsic volume fractions, the population 1, 2 and 3 surface areas per unit sample volume, together with their total, extracted directly from the MaxEnt size distributions, have been normalized by dividing by a factor $(1 - \Phi_{V4})$ where Φ_{V4} is the directly obtained population 4 vol fraction. Once again, this removes effects simply due to less than complete packing of the pressed powdered clay samples, and provides the intrinsic surface areas per true montmo-

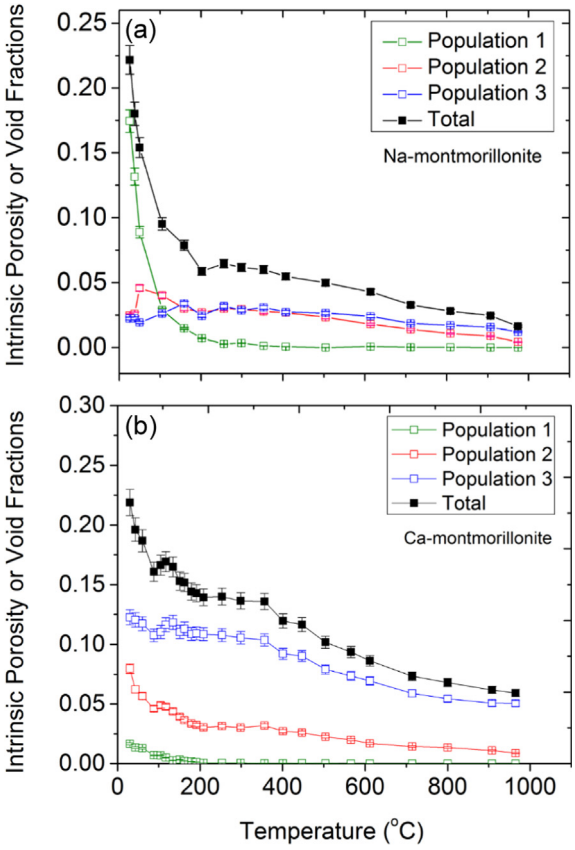

Fig. 9. Intrinsic porosities or void fractions of (a) Na-montmorillonite and (b) Ca-montmorillonite populations 1, 2 & 3, with respect to true sample volume after pore population 4 is subtracted out, on heating from 30 °C to 1000 °C. Vertical bars where visible represent estimated standard uncertainties.

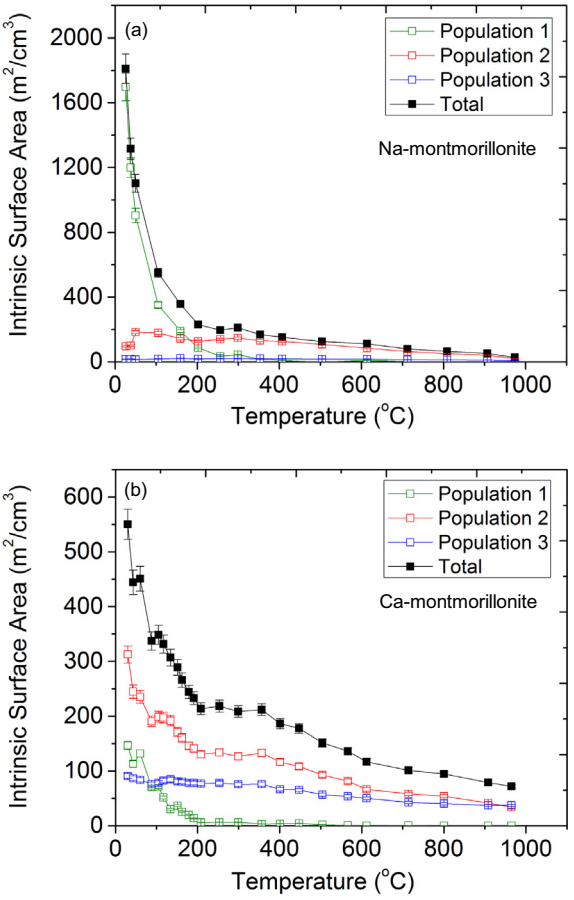

Fig. 10. Intrinsic surface areas of (a) Na-montmorillonite and (b) Ca-montmorillonite populations 1, 2 and 3, with respect to true sample volume after pore population 4 subtracted out, on heating from 30 °C to 1000 °C. Vertical bars where visible represent estimated standard uncertainties.

rillonite sample volume. The Na-montmorillonite intrinsic surface areas are much greater than those for Ca-montmorillonite. At ambient temperature, the surface areas of Na-montmorillonite and Ca-montmorillonite are 1840 m^2/cm^3, and 550 m^2/cm^3, respectively. In Na-montmorillonite at ambient temperature, population 1 corresponds to 93% of the overall surface area, while populations 2 and 3 account for the rest. The surface areas of the pores that correspond to populations 1, 2, and 3 are (1710, 120 and 10) m^2/cm^3, respectively. In contrast, the intrinsic surface areas of populations 1, 2, and 3 in Ca-montmorillonite are (150, 310 and 95) m^2/cm^3, respectively.

In Na-montmorillonite and Ca-montmorillonite, the significant reductions in the overall surface area correspond to the removal of the interlayer water on heating to 200 °C. Furthermore, the contributions of the meso-scale structures (populations 2 and 3) to the overall surface area are greater in Ca-montmorillonite compared to Na-montmorillonite. At (974 and 965) °C, the total intrinsic surface areas of the pores in Na- and Ca-montmorillonite are only (1.5 and 13.1)% of the starting surface areas under ambient conditions. Significant reductions in the void fractions and surface areas on heating to 1000 °C and beyond indicate sintering effects in these materials [3].

4.1.3. Morphological changes in Na- and Ca-montmorillonite on heating from 1000 °C to 1150 °C

The maximum entropy based population models used to calculate the morphological properties of Na- and Ca-montmorillonite at temperatures below 1000 °C do not capture the changes in the morphology well when these clays are heated to higher temperatures. We have found that assuming a fractal morphology is more effective in describing the high-temperature microstructural changes that can be associated with the phase transitions reported in the literature [73,74] and confirmed by the structural changes in clays at these temperatures (Figs. 4 and 5). The disordered morphological character of Na-montmorillonite and Ca-montmorillonite at these temperatures is best captured by the correlation lengths, dimensions of the fractal features, their volume fractions, and the observed fractal exponents.

The combined USAXS/SAXS data for temperatures above 1000 °C can be modeled with combined volume-fractal and surface-fractal models. However, as the temperature is further increased, the volume-fractal component becomes stunted with an unrealistically high fractal exponent, D_V, and a correlation length, ξ_V, comparable with the fundamental pore building block size. Thus, a significant decrease in the volume fraction and surface area of the volume-fractal morphology in Na-montmorillonite is found on heating above 1040 °C (Fig. 11(a)) from the collapse of the correlation length corresponding to the volume-fractal. While the initial volume-fractal morphology in Ca-montmorillonite is not as prominent compared to that in Na-montmorillonite, the decrease in the correlation length occurs only at temperatures >1090 °C. In both Na- and Ca-montmorillonite, the surface-fractal correlation lengths are greater for temperatures >1050 °C. Indeed, on increasing the temperature in excess of 1100 °C the microstructure can be characterized by a development of surface-fractal morphology and a collapse of the volume-fractal morphology in both montmorillonite systems. Furthermore, for temperatures >1000 °C, the representative mean oblate fine pore dimension and the associated correlation hole radii (nearest neighbor distances) continue to increase with temperature (Fig. 11(b)), and both of these dimensions are greater in Na- than in Ca-montmorillonite. This is consistent with the greater scattering intensities in Na-montmorillonite compared to Ca-montmorillonite at temperatures above 1000 °C (Figs. 2(d) and 3(d)).

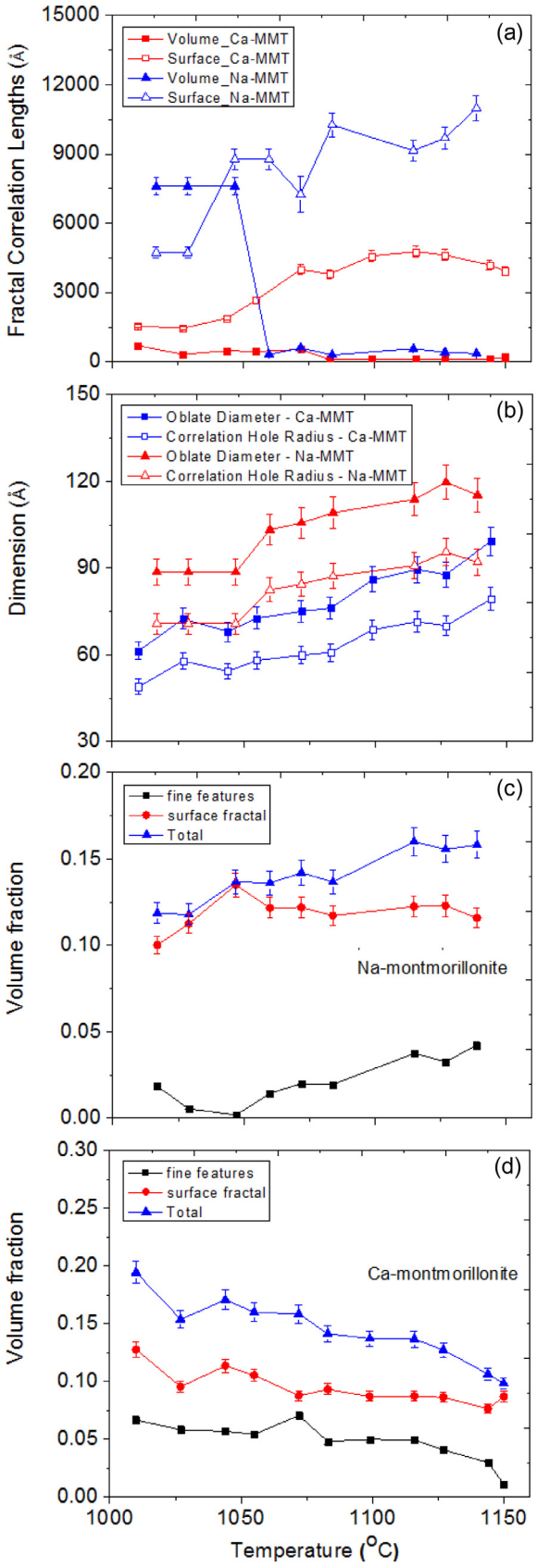

Fig. 11. Morphologies of Na-montmorillonite and Ca-montmorillonite at temperatures > 1000 °C based on fractal fits: (a) correlation lengths for volume- & surface-fractals; (b) oblate diameters & correlation hole radii; volume fractions of fine pore features and of surface-fractal morphology (estimates) for (c) Na-montmorillonite, and (d) Ca-montmorillonite. Vertical bars, where visible, represent estimated standard uncertainties in the fractal fits.

The dynamic changes in the fractal correlation lengths (Fig. 11 (a)), dimensions (Fig. 11(b)), and volume fractions (Fig. 11 (c) and (d)) in the temperature range of (1000–1150) °C are consistent with studies that indicate that this is a transition temperature regime prior to the development of well-defined mullite structures at temperatures >1200 °C [58]. The changes in the overall volume fractions of Na-montmorillonite and Ca-montmorillonite arising from the fine feature and surface-fractal volume fractions (Fig. 11 (c) and (d)) are in the range of the volume fractions found just below 1000 °C (as determined from the *MaxEnt* method) (Fig. 9). The continuous reductions in the volume fractions of Ca-montmorillonite (Fig. 11(c)) are indicated by the lower scattering intensities in USAXS (Fig. 3(a-4)), unlike the changes in Na-montmorillonite (Fig. 11(c)) where the scattering intensities are less sensitive to temperature changes (Fig. 2(a-4)).

4.2. Changes in the characteristic basal distance on heating Na-montmorillonite and Ca-montmorillonite to 1150 °C

The changes in the basal distances in both clays are quantified by shifts in q of the associated small-angle diffraction peak in our scattering measurements. Previous studies have reported that the basal distances in the presence of zero (0 W) and single-layer (1 W) hydrates of smectites are in the ranges: (9.5–10.2) Å and (11.6–12.7) Å, respectively [16,26–33]. As discussed in earlier sections, the basal distances of Na- and Ca-montmorillonite at the beginning of the experiment are 10.8 Å and 11.7 Å, respectively, which correspond to 0–1 W and 1 W hydrates, (Figs. 2(b-1) and 3 (b-1), and now summarized in Fig. 12). On heating from ambient temperature to 200 °C, the basal distances in Na-montmorillonite and Ca-montmorillonite change from (10.8–9.7) Å, and from (11.7–9.9) Å (Fig. 12). For clay sheets that correspond to sizes ≈ 6 Å, the corresponding interlayer space is ≈ 4–6 Å, which corresponds to the small dimensions of the spheroids from our morphology model. These results show that our morphological model is consistent with our quantitative results for the interlayer distances.

The conversion of the single layer to zero layer hydrates occurs on heating to temperatures in excess of 130 °C, which is consistent with other studies that have investigated the dehydration of montmorillonites [16]. On heating from 200 °C to 900 °C, the basal distances remain in the range of (9.6–9.9) Å in both Na- and Ca-montmorillonite, but the basal distance (001) diffraction peak completely disappears on heating beyond 1029 °C and 1010 °C in Na- and Ca-montmorillonite, respectively. These results are consistent with the major structural transitions reported for montmorillonites on heating [58].

The integrated basal distance diffraction peak intensities show analogous changes to the characteristic basal distance d-spacings. The assymetric peak profiles (themselves, sitting on the small-angle scattering from the swelling layer porosity) were fitted using a Gumbel peak function [75]. The integrated peak intensities reduced twofold to 0.02 cm^{-1} sr^{-1} $Å^{-1}$ and fourfold to 0.035 cm^{-1} - sr^{-1} $Å^{-1}$ on heating from 30 °C to 200 °C in Na-montmorillonite and Ca-montmorillonite, respectively. While the basal distance d-spacings persist on heating through the range: 200–900 °C, the integrated peak intensities progressively decrease through this range. The initial reductions in integrated peak intensities (below 200 °C) correspond to the significant reduction in the population 1 porosities in Fig. 9. However, some basal distance diffraction peak intensity persists to above 900 °C, indicating that the regularly spaced swelling layers remain even when the swelling layer water has been lost. The eventual disappearance of the basal distance diffraction peak in both montmorillonites occurs between 975 °C and 1050 °C, as shown in Fig. 12.

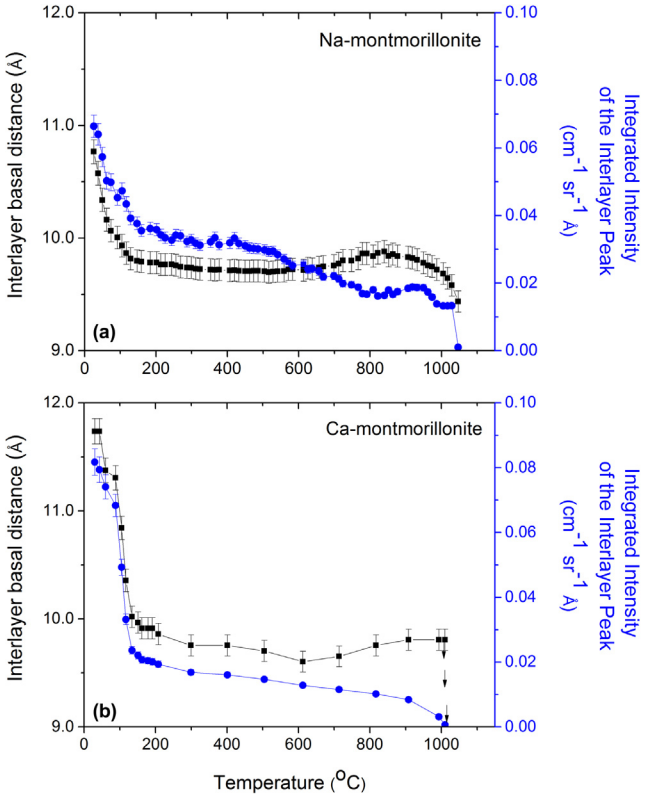

Fig. 12. Changes in the basal distances corresponding to the interlayer (d(001) peak) (a) and the integrated peak intensity (b) in Na-montmorillonite and Ca-montmorillonite on heating from 30 °C to 1150 °C. Vertical bars are standard deviation uncertainties obtained from the peak profile fitting.

4.3. Structural changes in Na- and Ca-montmorillonite on heating to 1150 °C

Unlike the intensities of the basal distance diffraction peak in Na- and Ca-montmorillonite, which are significantly reduced on heating to 200 °C (Fig. 12), changes in the intensities of the structural diffraction peaks of Na- and Ca-montmorillonite are more gradual (Fig. 13). Fig. 13 presents the integrated intensities of the selected characteristic montmorillonite peaks already shown in Fig. 4. The structural changes in the montmorillonite clays on heating, as represented by the integrated peak intensities, are relative to the starting states of the clays at ambient temperature. The results indicate that major structural changes occur in both montmorillonites for temperatures above 600 °C. This is consistent with the onset of significant dehydroxylation of the clay structure [54]. Only a small fraction of the original structure (as measured by the intensities of the selected peaks) remains present on heating to 900 °C.

Significant structural transitions in clays are known to occur at temperatures in excess of 1000 °C [3,58,73]. In our studies, the initial formation of mullite and cristobalite are evident on heating beyond 1000 °C as discussed in Section 3, and presented in Fig. 5. While the onset of mullite occurs between 1000 °C and 1150 °C, the growth of more distinctive mullite phases only starts in Ca-montmorillonite-rich clays at temperatures in excess of 1200 °C [58]. The fractal morphology of the clays in this transitional range [73] has been presented, modeled and discussed previously in Section 4.1.3. Here, we simply note that Fig. 13 shows clearly that, following the loss of swelling pore water below 200 °C, the other two major transformation onsets in both montmorillonites occur for temperatures above 600 °C (major dehydroxylation) and above

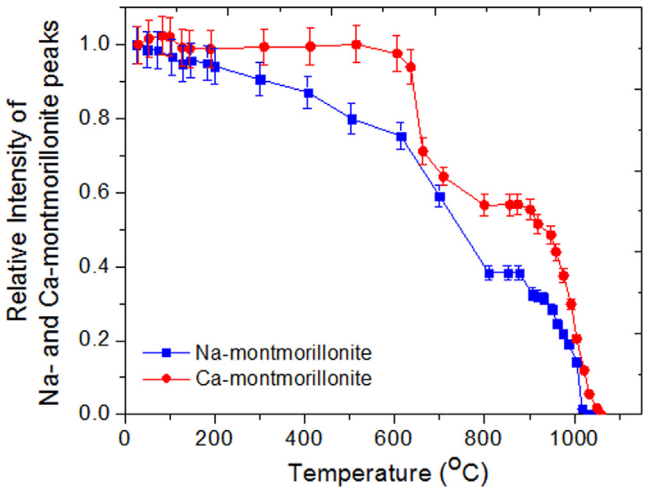

Fig. 13. Changes in normalized integrated peak intensities of selected characteristic peaks in (a) Na-montmorillonite, and (b) Ca-montmorillonite. Vertical bars represent estimated standard deviation uncertainties.

900 °C (loss of clay structure and eventual transformation to mullite).

5. Conclusions

In-operando multi-scale X-ray characterization of the heat treatment of Na- and Ca-montmorillonite across spatial scales that range from Å to μm and a temperature scale ranging from 30 °C to 1150 °C provides comprehensive microstructural and structural insights into clay systems. At the microstructural level, significant reductions in the porosity of the clays on heating are noted that are consistent with the known sintering behaviors of clays at temperatures above 800 °C. At the nano-structural level, the characteristic basal distance is reduced by the removal of water on heating to 200 °C, and there is a complete removal of the regular interlayer repeat structure at temperatures above 1000 °C – consistent with sintering effects of structural rearrangement. Notably, between 200 °C and 1000 °C, despite the pore volume with thickness of 3–4 Å being greatly reduced, the basal (001) diffraction peak persisted, which indicates that the layered structure is maintained despite changes in the interlayer pore spacing. At the Å-scale, heating to 1000 °C results in the gradual dehydroxylation of the structure of the montmorillonite clays coupled with the onset of new phases such as mullite. Different cations intercalated in the clay interlayer result in differences in the nano- and meso-scale morphology. We identified that the Na-montmorillonite intrinsic surface areas are much greater than those for Ca-montmorillonite. Our investigations show that Ca^{2+} interlayer cations confer more defined morphological regimes compared to Na^{+} ions, as evident from the USAXS curves, and produce subtle differences in the crystal structural changes at elevated temperatures.

Acknowledgements

The authors gratefully acknowledge Dr. Jan Ilavsky, X-ray Science Division, Argonne National Laboratory, for providing experimental support for the combined USAXS/SAXS/WAXS measurements at the Advanced Photon Source. The use of the Advanced Photon Source, an Office of Science User Facility operated for the U.S. Department of Energy (DOE) Office of Science by Argonne National Laboratory, is supported by the U.S. DOE under Contract DE-AC02-06CH11357.

Appendix A. Supplementary material

Supplementary data associated with this article can be found, in the online version, at http://dx.doi.org/10.1016/j.fuel.2017.01.092.

References

[1] Maitland G. Curr Opin Colloid Interface Sci 2000;5(5–6):301–11.
[2] Yong RN, Pusch R, Nakano M. Containment of high-level radioactive and hazardous solid wastes with clay barriers. CRC Press; 2009.
[3] Carter CB, Norton MG. Ceramic materials: science and engineering. Springer Science & Business Media; 2007.
[4] Hao F, Zou H, Lu Y. Am Assoc Pet Geol Bull 2013;97(8):1325–46.
[5] Javadpour F, Fisher D, Unsworth M. J Can Pet Technol 2007;46:10.
[6] Bailey SE, Olin TJ, Bricka RM, Adrian DD. Water Res 1999;33(11):2469–79.
[7] Pusch R. In: Intl Symp Soil Structure Proc; 1973.
[8] Sergeyev YM, Grabowska-Olszewska B, Osipov VI, Sokolov VN. Kolomenski., Y. N. J Microsc 1980;120(3):237–60.
[9] Chenu C, Tessier D. Scanning Microsc 1995;9(4):989–1010.
[10] Curtis ME, Sondergeld CH, Ambrose RJ, Rai CS. Am Assoc Pet Geol Bull 2012;96 (4):665–77.
[11] Bihannic I, Delville A, Demé B, Plazanet M, Villiéras F, Michot LJ. In: Neutron Applications in Earth. Energy and Environmental Sciences; 2009; p. 521–46.
[12] Busch A, Schweinar K, Kampman N, Coorn A, Pipich V, Feoktystov A, et al. In: Fifth EAGE Shale Workshop; 2016.
[13] Knudsen KD, Fossum JO, Helgesen G, Haakestad MW. Phys B Condens Matter 2004;352 (1):247–258.
[14] van Garderen N, Clemens FJ, Kaufmann J, Urbanek M, Binkowski M, Graule T, et al. Microporous Mesoporous Mater 2012;151:255–63.
[15] Ferrage E, Lanson B, Sakharov BA, Drits VA. Am Mineral 2005;90(8–9):1358–74.
[16] Ferrage E, Kirk CA, Cressey G, Cuadros J. Am Mineral 2007;92(7):994–1006.
[17] Bray HJ, Redfern SA, Clark SM. Mineral Mag 1998;62(5):647–56.
[18] Ilavsky J, Jemian PR, Allen AJ, Zhang F, Levine LE, Long GG. J Appl Crystallogr 2009;42(3):469–79.
[19] Ilavsky J, Zhang F, Allen AJ, Levine LE, Jemian PR, Long GG. Metall Mater Trans A 2013;44:68–76.
[20] Zhang F, Levine LE, Allen AJ, Campbell CE, Creuziger AA, Kazantseva N, et al. Acta Mater 2016;111:385–98.
[21] Radlinski AP. Rev Mineral Geochem 2006;63(1):363–97.
[22] Bahadur J, Radlinski AP, Melnichenko YB, Mastalerz M, Schimmelmann A. Energy Fuels 2015;29(2):567–76.
[23] Clarkson CR, Solano N, Bustin RM, Bustin AMM, Chalmers GRL, He L, et al. Fuel 2013;103:606–16.
[24] Meunier A. Clays. Springer Science & Business Media; 2005.
[25] Winans RE, Seifert S, Carrado KA. 2002, No. 6, 739–742.
[26] Ferrage E, Lanson B, Sakharov BA, Geoffroy N, Jacquot E, Drits VA. Am Mineral 2007;92(10):1731–43.
[27] Saiyouri N, Tessier D, Hicher PY. Clay Miner 2004;39(4):469–79.
[28] Svensson PD, Hansen S. Appl Clay Sci 2010;49(3):127–34.
[29] Kozaki T, Fujishima A, Sato S, Ohashi H. Nucl Technol 1998;121(1):63–9.
[30] Kozaki T, Sato H, Fujishima A, Sato S, Ohashi H. J Nucl Sci Technol 1996:33 (6):522–524.
[31] Tao L, Xiao-Feng T, Yu Z, Tao G. Chinese Phys B 2010;19(10):109101.
[32] Rutherford DW, Chiou CT, Eberl DD. Clays Clay Miner 1997;45(4):534–43.
[33] Boek ES, Coveney PV, Skipper NT. Langmuir 1995;11(12):4629–31.
[34] Nagelschmidt G. Zeitschrift Krist 1936;93:481–7.
[35] Bradley WF, Grim RE, Clark GF. Zeitschrift Krist 1937;97:216–22.
[36] Mooney RW, Keenan AG, Wood LA. J Am Chem Soc 1952;74:1371–4.
[37] Norrish K. Discuss Faraday Soc 1954;18:120–34.
[38] Harward ME, Brindley GW. Clays Clay Miner 1965;13:209–22.
[39] Harward ME, Carstea DD, Sayegh AH. Clays Clay Miner 1969;16:437–47.
[40] Watanabe T, Sato T. Clay Sci 1988;7:129–38.
[41] Sato T, Watanabe T, Otsuka R. Clays Clay Miner 1992;40:103–13.
[42] Yamada H, Nakazawa H, Hashizume H, Shimomura S, Watanabe T. Clays Clay Miner 1994;42:77–80.
[43] Tamura K, Yamada H, Nakazawa H. Clays Clay Miner 2000;48:400–4.
[44] Ferrage E, Lanson B, Malikova N, Plançon A, Sakharov BA, Drits VA. Chem Mater 2005;17:3499–512.
[45] Ferrage E, Lanson B, Sakharov BA, Drits VA. Am Mineral 2005;90:1358–74.
[46] Ilavsky J, Jemian PR. J Appl Crystallogr 2009;42(2):347–53.
[47] Ilavsky J. J Appl Crystallogr 2012;45(2):324–8.
[48] Segad M, Hanski S, Olsson U, Ruokolainen J, Åkesson T, Jönsson B. J Phys Chem C 2012;116(13):7596–601.
[49] Favejee JCL. Zeitschrift für Krist Mater 1939;100:425–36.
[50] Gruner JW. Am Mineral 1935;20(7):475–83.
[51] Nadeau PH. Clay Miner 1985;20(4):499.
[52] Mering J. Oberlin A. In: Gard JA, editor. The Electron-Optical investigation of Clays. London, UK: Mineralogical Society; 1971. p. 193–229.
[53] Brindley GW. In: Brown, GWBG, editor, Crystal structures of clay minerals and their X-ray identification. London (UK): Mineralogical Society; 1980. p 125–195.
[54] Grim RE, Bradley WF. J Am Ceram Soc 1939;23(8):242–8.
[55] Hyslop JF, Rooksby HP. J Soc Glas Technol 1926;10:412–6.

[56] McVay TN, Thompson CL. J Am Ceram Soc 1928;11(11):829–41.
[57] Hanawalt JD, Rinn HW, Frevel LK. Ind Eng Chem Anal Ed 1938;10:457–512.
[58] McConville CJ, Lee WE. J Am Ceram Soc 2005;88(8):2267–76.
[59] Schneider H, Schreuer J, Hildmann B. J Eur Ceram Soc 2008;28(2):329–44.
[60] Rehak P, Kunath-Fandrei G, Losso P, Jäger C, Hildmann B, Schneider H. Am Mineral 1998;83(12):1266–76.
[61] Glatter O, Kratky O. Small angle scattering. New York: Academic; 1982.
[62] Porod G. Kolloid Z. 1951;124:83–114.
[63] Porod G. Kolloid Z. 1952;125:108–22.
[64] Potton JA, Daniell GJ, Rainford BD. J Appl Crystallogr 1988;21(6):663–8.
[65] Morrison JD, Corcoran JD, Lewis KE. J. Appl. Crystallogr. 1992;25(4):504–513. (65a) Jemian, PR, Allen AJ. J Appl Crystallogr 1994;27:693–702.
[66] Mandelbrot BB. Fractals. John Wiley & Sons Inc; 1977.
[67] Mandelbrot BB. WH Free. Co., New York; 1982, 1(983), 1.
[68] Pfeifer P, Avnir D. J Chem Phys 1983;79(7):3558–65.
[69] Freltoft TJKSK, Kjems JK, Sinha SK. Phys Rev B 1986;33(1):269.
[70] Bale HD, Schmidt PW. Phys Rev Lett 1984;53(6):596.
[71] Michot LJ, Bihannic I, Porsch K, Maddi S, Baravian C, Mougel J, et al. Langmuir 2004;20(25):10829–37.
[72] Cadene A, Durand-Vidal S, Turq P, Brendle J. J Colloid Interface Sci 2005;285(2):719–30.
[73] Zhang X, Liu X, Meng G. J Am Ceram Soc 2005;88(7):1826–30.
[74] Eggersdorfer ML, Kadau D, Herrmann HJ, Pratsinis SE. Langmuir 2011;27(10):6358–67.
[75] Gumbel EJ. Statistical theory of extreme values and some practical applications. Applied Mathematics Series. 33 (1st ed.); National Bureau of Standards. ASIN B0007DSHG4; 1954.